Metal−Insulator Transitions, Structural and Microstructural Evolution of $RNiO_3$ (R = Sm, Eu, Gd, Dy, Ho, Y) Perovskites: Evidence for Room-Temperature Charge Disproportionation in Monoclinic $HoNiO_3$ and $YNiO_3$

José A. Alonso,* María J. Martínez-Lope, María T. Casais, Miguel A. G. Aranda, and María T. Fernández-Díaz

Contribution from the Instituto de Ciencia de Materiales de Madrid, C.S.I.C., Cantoblanco, E−28049 Madrid, Spain, Departamento de Química Inorgánica, Cristalografía y Mineralogía, Facultad de Ciencias, Universidad de Málaga, E−29071 Málaga, Spain, and Institut Laue-Langevin, B.P. 156, 38042 Grenoble Cedex 9, France

Received November 20, 1998

Abstract: $RNiO_3$ nickelates have been prepared under high oxygen pressure (R = Sm, Eu, Gd) or high hydrostatic pressure (R = Dy, Ho, Y) in the presence of $KClO_4$. The samples have been investigated at room temperature (RT) by synchrotron X-ray powder diffraction to follow the evolution of the crystal structures and microstructures along the series. The distortion of the orthorhombic (space group *Pbnm*) perovskite progressively increases along the series, leading for the smallest Ho^{3+} and Y^{3+} cations to a subtle monoclinic distortion (space group $P2_1/n$) which implies the splitting of the Ni positions in the crystal. This symmetry was confirmed by neutron powder diffraction; the crystal structures for R=Ho and Y were refined simultaneously from RT synchrotron and neutron powder diffraction data. In both perovskites the oxygen octahedra around Ni1 and Ni2 positions are significantly distorted, suggesting the manifestation of Jahn−Teller effect, which is almost absent in the nickelates of lighter rare earths. The very distinct mean Ni−O bond distances observed for Ni1 and Ni2 atoms at RT, in the insulating regime, suggest the presence of a charge disproportionation effect, considered as driving force for the splitting of the Ni positions. The metal−insulator (MI) transitions for $RNiO_3$ (R = Gd, Dy, Ho, Y), above room temperature, have been characterized by DSC. The transition temperatures for Gd, Dy, Ho, and Y oxides in the heating runs are 510.7, 563.9, 572.7, and 581.9 K, respectively. The increasing rate of T_{MI} for Dy, Ho, and Y materials is lower than that expected from the variation of T_{MI} for the larger rare earth perovskites. This is probably related to the subtle monoclinic distortion found for Ho and Y nickelates. The high-resolution synchrotron X-ray powder patterns have revealed changes in the microstructure along the series. Powder patterns for orthorhombic $RNiO_3$ (R = Sm, Eu, Gd, Dy) display asymmetric tails for some reflections which are due to structural mistakes such as stacking faults or regular intergrowths. These mistakes are not present in monoclinic $RNiO_3$ (R=Ho, Y) nickelates.

Introduction

The discovery of thermally driven metal−insulator (MI) transitions in the $RNiO_3$ perovskites (R = rare earth)[1] has stimulated intense research efforts. These paradigmatic oxides are the best opportunity known so far to investigate the closing of the charge-transfer gap in structurally simple, undoped, narrow-band oxides. The transition temperature, T_{MI}, between the low-temperature insulating state and the high-temperature metallic state, rises systematically as the rare-earth size becomes smaller, i.e., as the distortion of the perovskite with respect to the ideal structure (aristotype) increases.[2−5] The existence of electronically induced subtle structural changes associated with the transition was reported earlier.[3] The interest in rare-eath nickelates has been reinforced after the discovery of an unexpected magnetic ordering in $PrNiO_3$ and $NdNiO_3$ associated with the electronic localization.[6] In these compounds the magnetic ground state consists of alternating ferromagnetic and antiferromagnetic Ni−O−Ni couplings that violate the inversion center at the Ni site. This suggests the existence of a nonuniform orbital distribution of the single e_g electron,[6] similar (but not equal) to that recently found in some insulating phases of manganese perovskites. However, thus far orbital ordering has not been observed from the anisotropy of the Ni−O bond distances in NiO_6 octahedra, even though low-spin Ni^{3+} ($t^6_{2g}e^1_g$) is as susceptible to undergoing the Jahn−Teller (JT) effect as Mn^{3+} ($t^3_{2g}e^1_g$) does in stoichiometric $LaMnO_{3.00}$. This is probably a manifestation of the higher covalent character of the Ni-mixed oxides because the larger crystal field in the nickelates makes the ionic picture less adequate than for the manganates. A recent neutron diffraction search for small nuclear superstructure peaks due to a possible orbital ordering

* Corresponding author. E-mail: jalonso@fresno.csic.es.

(1) Lacorre, P.; Torrance, J. B.; Pannetier, J.; Nazzal, A. I.; Wang, P. W.; Huang, T. C. *J. Solid State Chem.* **1991**, *91*, 225

(2) Torrance, J. B.; Lacorre, P.; Nazzal, A. I.; Ansaldo, E. J.; Niedermayer, Ch. *Phys. Rev. B* **1992**,*45*, 8209.

(3) García-Muñoz, J. L.; Rodríguez-Carvajal, J.; Lacorre, P.; Torrance, J. B. *Phys. Rev. B* **1992**, *46*, 4414.

(4) Alonso, J. A.; Martínez-Lope, M. J.; Rasines I. *J. Solid State Chem.* **1995**, *120*, 170.

(5) Medarde, M. *J. Phys.: Condens. Matter* **1997**, *9*, 1679.

(6) García-Muñoz, J. L.; Rodríguez-Carvajal, J.; Lacorre, P. *Phys. Rev. B* **1994**, *50*, 978.

10.1021/ja984015x CCC: $18.00
Published on Web 05/06/1999

on isotopically enriched $^{154}SmNiO_3$ and $^{153}EuNiO_3$ was carried out without success.[7]

More recently, another similarity with Mn perovskites has been observed. $RNiO_3$ also display unusually large isotopic shifts of T_{MI} ($T_{MI}(^{18}O) - T_{MI}(^{16}O) \approx 10$ K)[8] that confirm the importance of the electron−lattice coupling. This behavior suggests that the mechanism of the MI transition involves a strong electron−lattice interaction via Jahn−Teller polarons.

$RNiO_3$ oxides (R = Pr, Nd, Sm, Eu) are orthorhombic, crystallize in the perovskite-distorted $GdFeO_3$ structure (space group *Pbnm*) and exhibit MI transitions at 130 K (Pr), 200 K (Nd), 400 K (Sm), and 460 K (Eu).[2−4] For $PrNiO_3$ and $NdNiO_3$, T_{MI} coincides with the paramagnetic−antiferromagnetic transition (T_N), but for R = Sm or smaller rare-earth cations, T_N is lower than T_{MI}, leading to the existence of an intermediate regime in which $RNiO_3$ are in an insulating and paramagnetic state.

The difficulties found in the syntheses of $RNiO_3$ perovskites, inherent to the stabilization of Ni^{3+} cations, increase as the size of the rare-earth cation decreases. $SmNiO_3$ and $EuNiO_3$ could be prepared under high oxygen pressure up to 200 bar.[1,4] But for smaller rare earths the corresponding perovskites had not been prepared after the pioneering work of Demazeau et al.,[9] who synthezised them in a belt press under 60 kbar.

In the course of our current research on rare-earth nickelates, we have been able to prepare $GdNiO_3$[10] at very high O_2 pressure, and $DyNiO_3$, $HoNiO_3$, and $YNiO_3$ in a piston-cylinder press. These samples had not been prepared within the last 25 years, and nothing is known about their electronic and magnetic properties, metal−insulator transitions, or structural features. In this paper, we report DSC measurements, a synchrotron X-ray powder diffraction (SXRD) study for $RNiO_3$ (R=Sm, Eu, Gd, Dy), and a combined synchrotron and neutron powder diffraction study for R = Ho, Y. Although $SmNiO_3$ and $EuNiO_3$ have already been structurally characterized by XRD and NPD[1,4,7], we have decided to include them in the series because high-resolution SXRD reveals new sample-dependent microstructural features which had not been reported so far. The evolution of structure and microstructure along the series will be discussed. The present structural study deals with the room-temperature $RNiO_3$ (R = Sm, Eu, Gd, Dy, Ho, Y) phases, below the MI transition, i.e., in the insulating-paramagnetic regime. Here, we report full structural data for room-temperature monoclinically distorted rare-earth nickelates (R = Ho and Y) which implies the existence of two crystallographically independent nickel sites. Since the two NiO_6 octahedra have significantly different average bond distances, we suggest the presence of commensurate charge disproportionation effect in these astonishing materials. A preliminary result for $YNiO_3$ has already been advanced,[11] concerning the structural changes across the MI transition and the low-temperature magnetic structure.

Experimental Section

$RNiO_3$ (R = Sm, Eu, Gd) samples were prepared as black polycrystalline powders as described in detail elsewhere.[4,10] $SmNiO_3$ and $EuNiO_3$ were annealed at 1000 °C under 200 bar of oxygen pressure, whereas the stabilization of $GdNiO_3$ required more oxidizing conditions, at 850 °C under 900 bar of O_2. The high-temperature annealing time was 12 h, and then the samples were cooled to room temperature at a rate of 300 °C h^{-1}.

$RNiO_3$ (R = Dy, Ho, Y) required even more oxidizing synthetic conditions. About 1 g of a stoichiometric mixture of R_2O_3 and NiO was ground together with 0.3 g of $KClO_4$. The mixture was put into a gold capsule, sealed, and placed in a graphite heater. The reaction was carried out in a piston-cylinder press (Rockland Research Co.), at a pressure of 20 kbar for 20 min at 900 °C. The samples were quenched down to room temperature, and the pressure was then released. The products were washed in aqueous HNO_3 (0.1 M) to dissolve KCl coming from the decomposition of $KClO_4$ and eliminate small amounts of unreacted NiO and R_2O_3 and then dried in air at 150 °C for 1 h.

The products were initially characterized by laboratory XRD (Cu Kα, $\lambda = 1.5406$ Å) for phase identification and to assess phase purity. For the structural refinements, SXRD patterns for $RNiO_3$, R = Sm, Eu, Gd, Dy, Ho, and Y, were collected at the BM16 diffractometer of ESRF-Grenoble. The samples were loaded in a borosilicate glass capillary ($\phi = 0.5$ mm) and rotated during data collection. A short wavelength, $\lambda = 0.518056(3)$ Å, selected with a double-crystal Si (111) monochromator and calibrated with Si NIST ($a = 5.43094$ Å), was chosen to reduce the absorption and to get the highest instrumental intensity and resolution. The temperature inside the experimental hutch was 16 °C. The runs took about 3 h to have good statistics over the angular range 6−43° in 2Θ. The data from the nine detectors were normalized and summed up to 0.005° step size with local software to produce the final raw "treatable" data. The standard geometrical configuration "Debye−Scherrer" was used. The size of the beam on sample was measured with a film, giving ~8.0 mm width and ~0.8 mm height. NPD patterns for $HoNiO_3$ and $YNiO_3$ were collected at room temperature at D2B high-resolution neutron diffractometer of ILL-Grenoble. The high-resolution mode was used for $HoNiO_3$, the high-flux mode for $YNiO_3$. A wavelength of ~1.6 Å was selected from a Ge monochromator. The value of the neutron wavelength was refined in the simultaneous analysis of the SXRD and NPD data sets by the Rietveld[12] method, using the GSAS refinement program.[13] A pseudo-Voigt function was chosen to generate the line shape of the diffraction peaks. No regions were excluded in the refinement. Depending on the sample, small amounts of Au (from the gold capsule), unreacted NiO or R_2O_3 were detected in the patterns. Then, the profile refinement of the mixture was performed. In the final run the following parameters were refined: histogram scale factor(s), background coefficients, zero-point error(s), unit-cell parameters, pseudo-Voigt corrected for asymmetry[14] parameters, phase fraction(s), positional coordinates, and isotropic thermal factors. The unit-cell parameters and the coefficients to fit the peak shape for the secondary phases were also refined. Combined SXRD and NPD refinements were performed for $RNiO_3$, R = Ho and Y.

Differential scanning calorimetry (DSC) experiments were performed in a Mettler TA3000 system equipped with a DSC30 unit, in the temperature range 300−863 K. The heating rate in both warming and cooling runs was 10 °C min^{-1}, using about 70 mg of sample in each run.

Results

$RNiO_3$, R = Sm, Eu, Gd, Dy, Ho, and Y samples, have been obtained as black, well-crystallized powders. The laboratory XRD diagrams are shown in Figure 1. The patterns are characteristic of strongly distorted perovskites showing sharp, well-defined superstructure reflections. The structural refinement was performed from SXRD data in the conventional *Pbnm* orthorhombic model, with unit-cell parameters related to $\mathbf{a_0}$

(7) Rodríguez-Carvajal, J.; Rosenkranz, S.; Medarde, M.; Lacorre, P.; Fernández-Díaz, M. T.; Fauth, F.; Trounov, V. *Phys. Rev. B* **1998**, *57*, 456.

(8) Medarde, M.; Lacorre, P.; Conder, K.; Fauth, F.; Furrer, A. *Phys. Rev. Lett.* **1998**, *80*, 2397.

(9) Démazeau, G.; Marbeuf, A.; Pouchard P.; Hagenmuller, P. *J. Solid State Chem.* **(1971**, *3*, 582.

(10) Alonso, J. A.; Martínez-Lope, M. J.; Casais, M. T.; Démazeau, D.; Largeteau, A.; García-Muñoz, J. L.; Fernández-Díaz, M. T., manuscript in preparation.

(11) Alonso, J. A.; García-Muñoz, J. L.; Fernández-Díaz, M. T.; Aranda, M. A. G.; Martínez-Lope, M. J.; Casais, M. T. *Phys. Rev. Lett.*, submitted for publication.

(12) Rietveld, H. M. *J. Appl. Crystallogr*. **1969**, *2*, 65.

(13) Larson, A. C.; von Dreele R. B. *(Program version: PC-98). Los Alamos National Lab. Rep.* No. LA-UR-86-748, **1994**.

(14) (a) Finger, L. W.; Cox, D. E.; Jephcoat, A. P. *J. Appl. Crystallogr*. **1994**, *27*, 892. (b) Aranda, M. A. G.; Losilla, E. R.; Cabeza, A.; Bruque, S. *J. Appl. Crystallogr*. **1998**, *31*, 16.

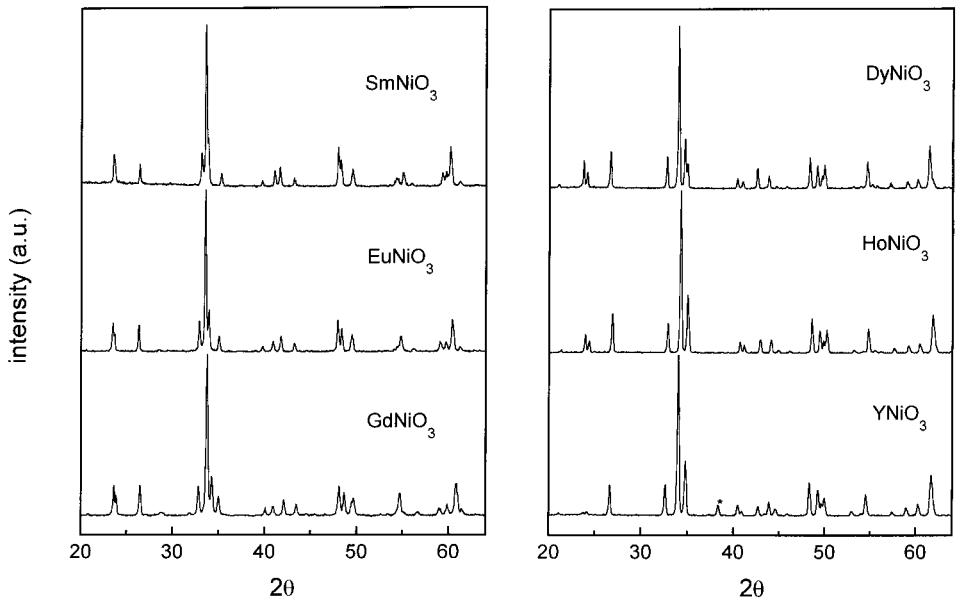

Figure 1. Laboratory XRD patterns for $RNiO_3$, R = Sm, Eu, Gd, Dy, Ho and Y. The star corresponds to Au from the gold capsule.

Table 1. Unit-Cell, Positional, Thermal Parameters and Reliability Factors for the Refinements of $RNiO_3$ Phases, in the Orthorhombic *Pbnm* Space Group, $Z = 4$, from SXRD Data at 289 K

R		Sm	Eu	Gd	Dy	Ho	Y
a (Å)		5.32693(6)	5.29413(6)	5.26063(5)	5.20836(5)	5.18202(5)	5.17922(4)
b (Å)		5.43283(6)	5.45857(6)	5.48544(5)	5.50536(5)	5.51046(5)	5.51509(4)
c (Å)		7.56483(9)	7.53710(8)	7.51116(7)	7.44700(7)	7.42347(7)	7.41602(6)
V (Å^3)		218.929(6)	217.810(6)	216.749(5)	213.535(4)	211.979(5)	211.830(2)
R	4*c*(*x y* 1/4)						
x		0.9899(2)	0.9872(1)	0.9850(1)	0.9826(1)	0.9818(1)	0.9820(2)
y		0.0514(1)	0.0574(1)	0.06307(9)	0.06915(8)	0.07164(9)	0.0728(1)
$10^2 \cdot U_{iso}$ (Å^2)		0.46(2)	0.37(2)	0.44(1)	0.47(1)	0.52(2)	0.55(3)
Ni	4*b*(1/2 0 0)						
$10^2 \cdot U_{iso}$ (Å^2)		0.27(4)	0.19(3)	0.33(5)	0.43(3)	0.39(3)	0.52(4)
O1	4*c*(*x y* 1/4)						
x		0.0825(16)	0.0890(14)	0.0885(12)	0.0969(12)	0.0972(15)	0.0978(13)
y		0.4865(14)	0.4767(13)	0.4765(12)	0.4699(12)	0.4676(15)	0.4717(11)
$10^2 \cdot U_{iso}$ (Å^2)		0.80(25)	0.23(21)	0.25(18)	1.12(18)	0.80(20)	0.72(18)
O2	8*d*(*x y z*)						
x		0.7086(11)	0.7058(11)	0.7038(9)	0.6946(8)	0.6923(11)	0.6920(9)
y		0.2932(11)	0.2947(10)	0.2974(9)	0.3029(9)	0.3033(11)	0.3045(9)
z		0.0457(8)	0.0444(7)	0.0471(7)	0.0491(6)	0.0516(8)	0.0519(7)
$10^2 \cdot U_{iso}$ (Å^2)		0.295(16)	0.13(15)	0.44(13)	0.36(12)	0.88(15)	0.88(14)
reliability factors							
χ^2		8.189	6.040	3.920	2.345	3.084	2.153
R_p		0.112	0.095	0.090	0.075	0.093	0.099
R_{wp}		0.145	0.120	0.112	0.093	0.118	0.120
R_1		0.050	0.042	0.039	0.028	0.030	0.049

(ideal cubic perovskite, $\mathbf{a_0} \approx 4$ Å) as $\mathbf{a} \approx \sqrt{2}\mathbf{a_0}$, $\mathbf{b} \approx \sqrt{2}\mathbf{a_0}$, $\mathbf{c} \approx 2\mathbf{a}_0$, using as starting models the structure already reported for $SmNiO_3$.[1] The final atomic coordinates, unit-cell parameters, and discrepancy factors for the refinements in the orthorhombic model are given in Table 1. The weight fraction of the main phase was higher than 92% for all samples. Sm nickelate was a pure single phase by SXRD. Eu sample was 98.7% $EuNiO_3$ with 1.3% of Eu_2O_3. Gd nickelate was 96.4% with 3.6% of Gd_2O_3. Dy sample was 92.2% with 6.6% of $Dy_2O_2CO_3$ and 1.2% of NiO. Ho nickelate was 99.5% with 0.5% of Au. Y sample was 95.5% with 2.0% of Au and 2.5% of NiO.

Microstructural Features. A close examination of the high-resolution SXRD profiles showed two types of special features which are highlighted in Figures 2 and 3. Figure 2 shows enlarged views (22.0−23.0°, 2Θ) of the raw SXRD patterns for $GdNiO_3$ and $HoNiO_3$ perovskites, and Figure 3 shows enlarged views (10.7−11.6°, 2Θ) of the raw SXRD patterns for $SmNiO_3$ and $HoNiO_3$ pervoskites, which are representative of the two types of observed diffractograms. For larger rare-earth nickelates (Sm, Eu, Gd, Dy) the patterns present anisotropic peak broadening. Full width at half maximum (fwhm) for selected reflections are given in Table 2. As it is shown in Figure 2 (and as it is given in Table 2), fwhm is larger for (041) [0.068°] than for (224) [0.041°] for R = Gd, Sm, and Eu nickelates. However, for R = Ho, fwhm is 0.042° for (041), much smaller than that for larger rare-earth nickelates, and the patterns (R = Ho, Y) almost do not show anisotropic peak broadening. The main peak of this region ((224) of *Pbnm*) is clearly split, indicating a lowering in symmetry: a monoclinic distortion develops for R = Ho, Y, as described in detail in the next section. Of these strongly overlapped two peaks [($22\bar{4}$), (224)], fwhm is only slightly larger, 0.054°, indicating a very subtle structural distortion. The peak shape anisotropy for R = Dy pattern is intermediate between these two limiting cases.

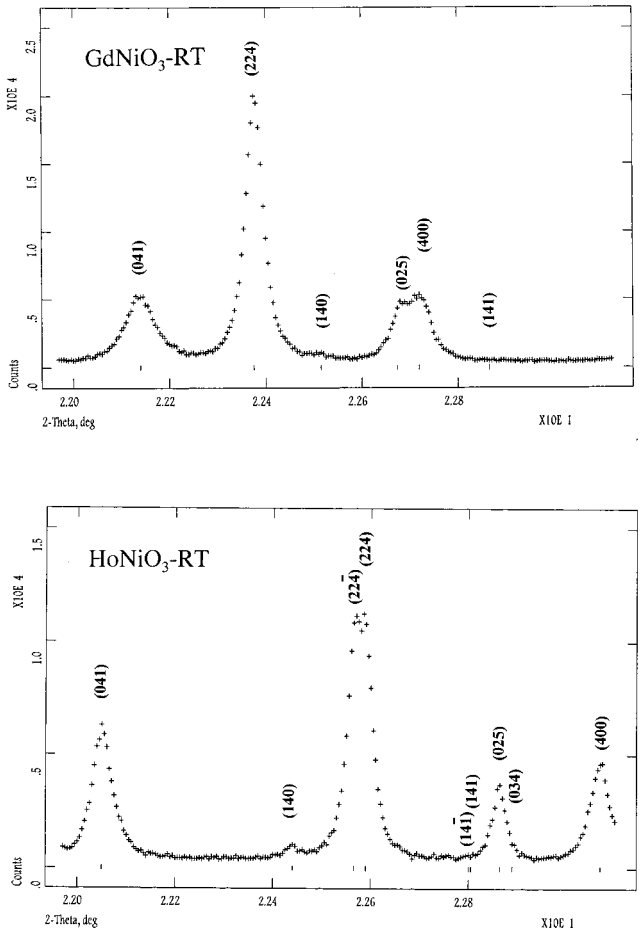

Figure 2. Selected angular region of the raw SXRD patterns for $GdNiO_3$ and $HoNiO_3$. The reflections are indexed according to orthorhombic and monoclinic unit cells, respectively.

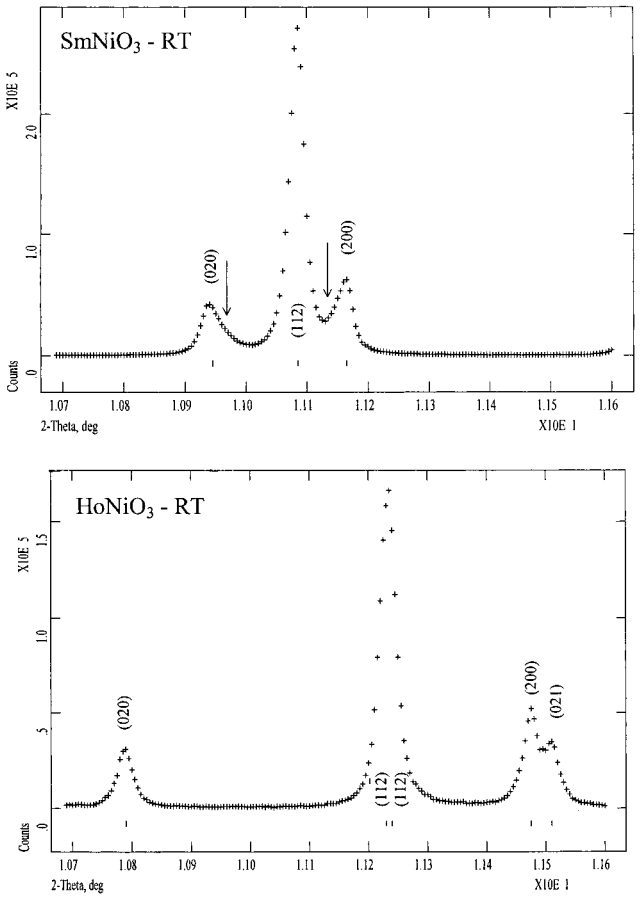

Figure 3. Selected angular region of the raw SXRD patterns for $SmNiO_3$ and $HoNiO_3$. The reflections are indexed, and the arrows indicate the asymmetric tails.

Table 2. Variation of fwhm (deg) for Selected Reflections in the $RNiO_3$ Series

	Sm	Eu	Gd	Dy	Ho	Y	2Θ (deg)	d^* (Å^{-1})
(020)	0.038	0.042	0.038	0.039	0.029	0.028	∼10.9	∼0.37
(220)	0.029	0.031	0.032	0.034	0.027	0.026	∼15.7	∼0.53
(004)	0.028	0.030	0.030	0.035	0.027	0.026	∼15.9	∼0.53
(041)	0.062[a]	0.071	0.063	0.063	0.041	0.034	∼22.2	∼0.75

[a] Value for (040) reflection as the (041) diffraction peak is overlapped.

For (041) and (224) reflections fwhms are 0.063, 0.053°, respectively.

The peak width due to the instrumental contribution was only ∼0.006° in the operating conditions. Then, fwhm of the observed diffractions peaks were invariably dominated by sample-dependent effects. The Gaussian contribution to the peak shape was very small, GW ≈ 0.5 [(0.01°)^2 units]. The Lorentzian contribution was very high with LY ≈ 15 [0.01° units]. No noticeable Lorentzian−Scherrer broadening was detected in the patterns, and Lorentzian broadening due to strains was very dominant. Figure 3 shows an enlarged low-angle region of the SXRD patterns for $SmNiO_3$ and $HoNiO_3$, and asymmetric tails for some reflections are evident and underlined. These tails are located both at the right part of some peaks, such as (020) and (131), or at the left part of other type of reflections, such as (200) or (311). The anisotropic peak broadening is mainly due to these tails which are originated by structural faults or mistakes. It is not possible to properly model these features with the existing software as it affects a particular class of reflections. As well, the ellipsoidal-type anisotropic correction of most of the existing Rietveld codes does not correct for this effect. In fact, it has not been possible to model the tails, which result in higher R factors for larger rare-earth perovskites (Table 1, Figure 3). We have used an anisotropic peak-broadening correction along the [010] direction in order to take into account part of this effect.

Figure 4 shows the variation of fwhm of unoverlapped reflections for $RNiO_3$ (R = Sm, Ho). The large spreading of the values of fwhm (for R = Sm, which is representative of the large rare-earth samples) indicates the complex microstructure of these materials. The situation is much simpler for R = Ho and Y where this spreading is not observed. There are fewer peaks in the R = Ho plot due to the monoclinic (strongly pseudo-orthorhombic) overlapping of many reflections. However, many doublets for R = Ho and Y such as $(22\bar{4})$ (224) still have lower fwhm values than single reflections with strong anisotropic tails.

Structural Features of Monoclinic $RNiO_3$ (R = Ho, Y) Perovskites. The splitting observed in some SXRD reflections for the most distorted perovskites, $HoNiO_3$ and $YNiO_3$, indicates a lowering in the crystal symmetry with respect to the orthorhombic *Pbnm* model (described in Table 1). Both structures have been successfully refined in the monoclinic $P2_1/n$ space group from SXRD data. $P2_1/n$ is a subgroup of *Pbnm*, hence, the monoclinic starting model was built using the refined orthorhombic structural parameters. In $P2_1/n$ it is necessary to define two crystallographically independent Ni positions (Ni1 and Ni2), as well as three kinds of nonequivalent oxygen atoms (O1, O2, and O3) all in general (*x*,*y*,*z*) positions. The refinements in the monoclinic model for both $HoNiO_3$ and $YNiO_3$ showed

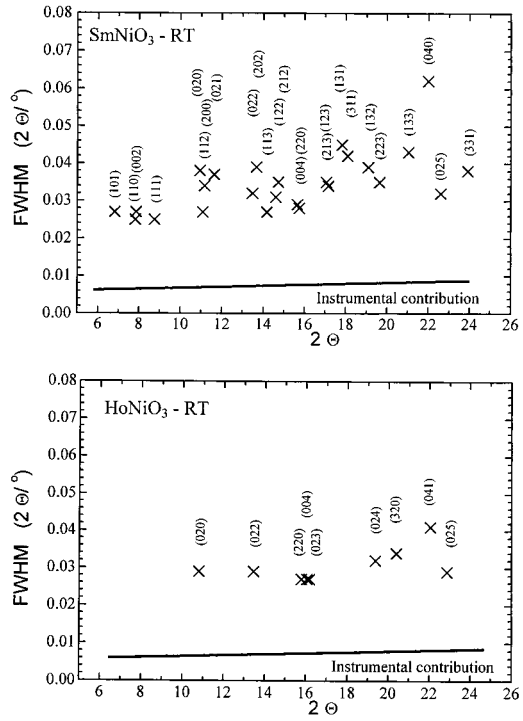

Figure 4. Variation of fwhm with 2Θ of single "unoverlapped" reflections for $SmNiO_3$ and $HoNiO_3$. The instrumental contribution to the fwhm of the peaks is also shown.

a significant improvement in reliability factors: as an example, χ^2 dropped from 3.08 to 1.97 for $HoNiO_3$, and from 2.15 to 1.83 for $YNiO_3$. The monoclinic β angle is, in both cases, very small, ~90.08°. The monoclinic model was tried for the remaining materials, with no significant improvement in the profile fittings for R = Sm, Eu, Gd, and Dy. Then, the metric of these structures seems to be orthorhombic although from a powder X-ray diffraction study, it is always difficult to assess the symmetry.

The monoclinically distorted perovskites, $HoNiO_3$ and $YNiO_3$, have three inequivalent oxygen positions, which cannot be very accurately determined by SXRD diffraction, as strong pseudosymmetry is present in the patterns. For this reason, neutron powder diffraction data were collected for both samples, neutrons being more sensitive to the oxygen positions. Despite the difficulties of such an experiment, given the relatively small amount of available sample (less than 0.8 g), two patterns with acceptable statistics could be collected and successfully refined. In the final study, a simultaneous SXRD and NPD refinement allowed optimization of all atomic positions. In Table 3 the unit-cell and atomic parameters and discrepancy factors corresponding to the combined refinement in the monoclinic model for $RNiO_3$, R = Ho and Y are given. To take into account differences in temperature for both data collections and as the neutron wavelength was not very accurately known, it was varied in the simultaneous refinement. The neutron wavelength converged to 1.59448(2) Å for R = Ho and 1.59438(2) Å for R = Y. Figure 5 shows the agreement between observed and calculated SXRD and NPD profiles for both perovskites after the combined refinements. Tables 4 and 5 contain selected bond distances and angles for orthorhombic (R = Sm, Eu, Gd, Dy) and monoclinic (R = Ho, Y) $RNiO_3$ perovskites.

Metal−Insulator Transitions. The MI transitions of $RNiO_3$ (R = Gd, Dy, Ho, Y) have been studied by DSC techniques. The heating process exhibits an endothermic peak corresponding to the insulator-to-metal transition. The reverse transition is observed during the cooling run, showing an exothermic peak. The endothermic and exothermic events are centered at slightly different temperatures, included in Table 6. The observed gain in energy (in the heating process) corresponds to the electronic delocalization when the rare earth nickelate reaches the metallic state, above T_{MI}.

Table 3. Unit-Cell, Positional, and Thermal Parameters for $HoNiO_3$ and $YNiO_3$ in the Monoclinic $P2_1/n$ Space Group, $Z = 4$, from Combined Refinements of SXRD and NPD Data at 289 K. Reliability Factors for Both Patterns Are also Given

R		Ho	Y
a (Å)		5.18200(4)	5.17932(5)
b (Å)		5.51050(4)	5.51529(5)
c (Å)		7.42336(5)	7.41656(7)
β (deg)		90.084(1)	90.081(1)
V (Å$_3$)		211.977(4)	211.857(5)
R	4e(x y z)		
x		0.98181(9)	0.9816(2)
y		0.07177(7)	0.0729(1)
z		0.2503(2)	0.2502(4)
$10^2 \cdot U_{iso}$ (Å^2)		0.47(1)	0.52(2)
Ni1 2d($^1/_2$ 0 0)			
$10^2 \cdot U_{iso}$ (Å^2)		0.36(7)	0.55(5)
Ni2 2c($^1/_2$ 0 $^1/_2$)			
$10^2 \cdot U_{iso}$ (Å^2)		0.34(7)	0.28(5)
O1	4e(x y z)		
x		0.0983(6)	0.0998(3)
y		0.4700(6)	0.4705(3)
z		0.2447(9)	0.2457(5)
$10^2 \cdot U_{iso}$ (Å^2)		0.63(7)	0.54(4)
O2	8d(x y z)		
x		0.700(1)	0.6973(7)
y		0.310(1)	0.3080(7)
z		0.0494(7)	0.0467(5)
$10^2 \cdot U_{iso}$ (Å^2)		0.50(12)	0.55(6)
O3	4d(x y z)		
x		0.187(1)	0.1882(6)
y		0.206(1)	0.2038(7)
z		0.9482(8)	0.9465(5)
$10^2 \cdot U_{iso}$ (Å^2)		0.63(12)	0.57(7)
reliability factors			
χ^2		1.679	1.691
synchrotron data			
R_p		0.077	0.092
R_{wp}		0.094	0.111
R_I		0.026	0.050
neutron data			
R_p		0.044	0.035
R_{wp}		0.054	0.043
R_I		0.051	0.030

Discussion

The structural parameters obtained for $SmNiO_3$ and $EuNiO_3$ are consistent with those previously reported from XRD and NPD studies.[1,4,7] A view of the crystal structure of $HoNiO_3$ is shown in Figure 6 to illustrate the main features of the monoclinically distorted perovskites. The structure is fairly distorted due to the small size of R^{3+} cations, which force the NiO_6 octahedra to tilt to optimize the R−O bond distances. Whereas in the orthorhombic perovskites there is only one kind of Ni^{3+} cations (i.e., all the NiO_6 octahedra are crystallographically and chemically equivalent), in monoclinic $HoNiO_3$ (and $YNiO_3$) there are two kinds of crystallographically and chemically different Ni^{3+} cations, which alternate along the three directions of the crystal, in such a way that each $Ni1O_6$ octahedra is linked to six $Ni2O_6$ octahedra, as shown in Figure 6, and vice versa.

Several examples of monoclinically distorted perovskites have been described in the past, for instance, $Nd_2(MgTi)O_6$,[15] Ca_2-

(15) Groen, W. A.; Van Berkel, F. P. F.; IJdo, D. J. W. *Acta Cryst. C* **1986**, *42*, 1472.

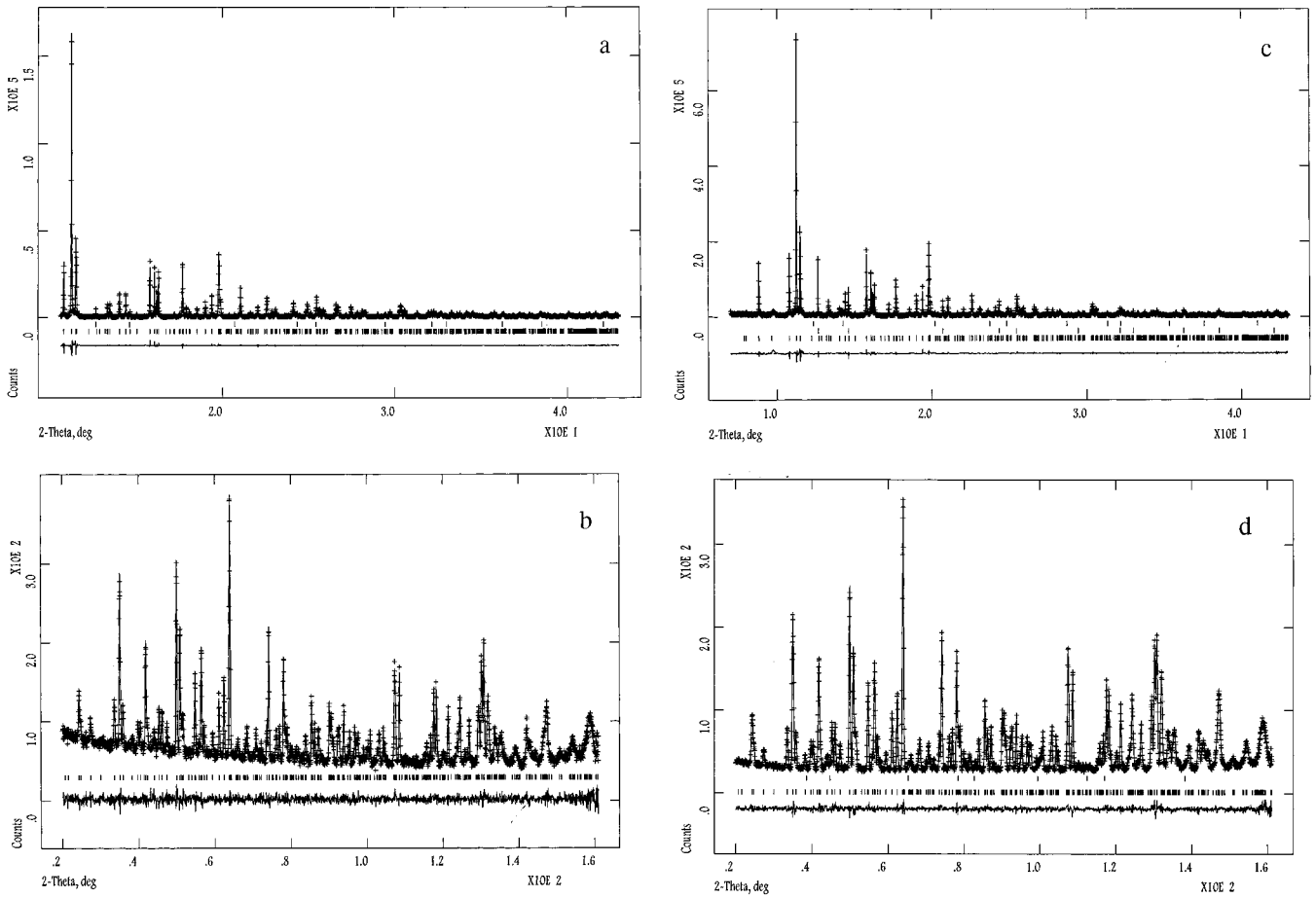

Figure 5. Observed, calculated, and difference profiles of the simultaneous SXRD and NPD refinements for (a) $HoNiO_3$, SXRD, (b) $HoNiO_3$, NPD, (c) $YNiO_3$, SXRD, and (d) $YNiO_3$, NPD.

Table 4. Main Bond Distances (Å) and Selected Angles (deg) for Orthorhombic $RNiO_3$ (R = Sm, Eu, Gd, Dy), Determined from SXRD Data at 289 K. The Distortion Parameter Δ_d for NiO_6 Octahedra with an Average Ni−O Distance $\langle d \rangle$ Is Defined as $\Delta_d = (1/6)\Sigma_{n=1,6}[(d_n - \langle d \rangle)/\langle d \rangle]^2$

R	Sm	Eu	Gd	Dy
NiO_6 octahedra				
Ni−O1 (×2)	1.943(2)	1.947(2)	1.939(2)	1.936(2)
Ni−O2 (×2)	1.973(6)	1.971(5)	1.984(5)	1.986(4)
Ni−O2 (×2)	1.947(6)	1.948(5)	1.946(5)	1.960(4)
⟨Ni−O⟩	1.954(4)	1.955(4)	1.956(4)	1.961(3)
$10^4\,\Delta_d$	0.46	0.32	1.02	1.08
Ni−O1−Ni (×2)	153.5(5)	150.9(4)	151.1(4)	148.1(4)
Ni−O2−Ni (×4)	152.1(3)	151.9(3)	150.4(3)	147.7(3)
⟨Ni−O−Ni⟩	152.6(4)	151.6(3)	150.6(3)	147.8(3)
RO_9 polyhedra				
R−O1	2.415(8)	2.351(7)	2.332(6)	2.285(6)
R−O1[a]	3.069(9)	3.082(8)	3.055(7)	3.068(6)
R−O1	2.305(9)	2.286(8)	2.293(7)	2.257(6)
R−O2 (×2)	2.522(7)	2.510(6)	2.483(6)	2.479(5)
R−O2 (×2)	2.340(5)	2.346(5)	2.331(5)	2.289(5)
R−O2 (×2)	2.660(7)	2.629(6)	2.625(6)	2.584(5)
$\langle R-O \rangle_{8\ short}$	2.471(7)	2.451(6)	2.438(6)	2.406(5)
⟨R−O⟩	2.537(7)	2.521(6)	2.506(6)	2.479(5)

[a] Long R−O distances.

$(CaU)O_6$,[16] $Sr_2(CaU)O_6$, and $Ba_2(SrU)O_6$.[17] In all of the cases the compounds crystallize in the $P2_1/n$ space group, with $\mathbf{a} \approx \mathbf{b} \approx \sqrt{2}\mathbf{a_0}$ and $\mathbf{c} \approx 2\mathbf{a_0}$, and they show long-range ordering between the two different cations placed at the B positions of the $A_2(BB')O_6$ perovskite structure. The driving force for the B, B′ ordering is the charge difference between both kinds of cations, for instance, Mg^{2+} and Ti^{4+} in $Nd_2(MgTi)O_6$ or Ca^{2+} and U^{6+} in $Ca_2(CaU)O_6$. It is remarkable that all of these compounds show an extraordinarily high pseudo-orthorhombic character as far as unit-cell dimensions are concerned: β angles are very close to 90°, e.g., $\beta = 90.010(9)°$ for $Nd_2(MgTi)O_6$.[15] However, the internal symmetry is monoclinic, as shown from neutron diffraction refinements.[15−17] This is also the case for $RNiO_3$, R = Ho, Y, which are metrically pseudo-orthorhombic ($\beta = 90.084(1)°$ for R = Ho, $\beta = 90.081(1)°$ for R = Y), but show a good and unique convergence in the $P2_1/n$ setting after the simultaneous refinement of SXRD and NPD data. As shown for $Nd(MgTi)O_6$, in $HoNiO_3$ and $YNiO_3$ (with nominal Ni^{3+} in the B-perovskite positions) the driving force for the monoclinic distortion leading to two independent positions for Ni is also the ordering between two differently charged Ni cations, as we will propose later, due to a charge disproportionation along the crystal.

It is important to point out that the very subtle monoclinic distortion present in R = Ho and Y materials has been detected because of the excellent resolution of SXRD data, as the instrumental contribution to the peak shape was virtually removed. In these conditions, sample-dependent effects such as the anisotropic tails due to structural mistakes and the monoclinic distortion were evident. The perovskite structures for $RNiO_3$ are very "strained" mainly due to the small size of the R^{3+} cations in the A site. The high-pressure synthetic conditions needed to stabilize Ni^{3+} may also be responsible, in

(16) Van Duivenboden, H. C.; Idjo, D. J. W. *Acta Crystallogr. C* **1986**, *42*, 523.
(17) Groen, W. A.; Idjo, D. J. W. *Acta Crystallogr. C* **1987**, *43*, 1033.

Table 5. Main Bond Distances (Å) and Selected Angles (deg) for Monoclinic $RNiO_3$ (R = Ho, Y), Determined from Combined SXRD and NPD Data at 289 K. Δ_d is Defined as in Table 3

R	Ho	Y
$Ni1O_6$ octahedra		
Ni1−O1 (×2)	1.970(6)	1.963(4)
Ni1−O2 (×2)	2.031(6)	2.012(4)
Ni1−O3 (×2)	2.015(6)	2.006(3)
⟨Ni1−O⟩	2.005(6)	1.994(4)
$10^4\,\Delta_d$	1.66	1.20
$Ni2O_6$ octahedra		
Ni2−O1 (×2)	1.893(6)	1.901(4)
Ni2−O2 (×2)	1.911(6)	1.924(3)
Ni2−O3 (×2)	1.927(7)	1.944(4)
⟨Ni2−O⟩	1.910(6)	1.923(4)
$10^4\,\Delta_d$	0.53	0.83
⟨Ni−O⟩	1.958(6)	1.959(4)
Ni1−O1−Ni2 (×2)	147.8(2)	147.4(1)
Ni1−O2−Ni2 (×2)	147.2(3)	147.9(2)
Ni1−O2−Ni2 (×2)	147.2(4)	146.5(2)
RO_9 polyhedra		
R−O1	2.276(3)	2.277(2)
R−O1[a]	3.058(3)	3.064(2)
R−O1	2.247(3)	2.241(2)
R−O2	2.466(6)	2.474(4)
R−O2	2.276(6)	2.295(4)
R−O2	2.573(6)	2.552(4)
R−O3	2.592(6)	2.597(4)
R−O3	2.298(7)	2.286(4)
R−O3	2.448(6)	2.440(4)
$\langle R-O\rangle_{8\ short}$	2.397(4)	2.395(3)
⟨R−O⟩	2.470(4)	2.470(3)

[a] Long R−O distances.

Table 6. Metal−Insulator Transition Temperatures (K) for $RNiO_3$, Obtained from DSC Curves in Both Cooling and Heating Runs

R	ref	T_{MI} heating	T_{MI} cooling
Pr	2	130	
Nd	2	200	
Sm	2	400	
Eu	4	462.5	458.6
Gd	this work	510.9	508.0
Dy	this work	564.1	560.6
Ho	this work	572.9	568.2
Y	this work	582.1	579.2

part, for the observed strain. For R = Sm, Eu, Gd, and Dy, the structures relaxed through structural mistakes such as stacking faults and intergrowths. However, for monoclinic (R = Ho and Y) perovskites there is no evidence of structural faults, the diffraction peaks being much narrower for these materials (Table 2, Figure 4). In this case, the reduction in symmetry from orthorhombic to monoclinic, with the concomitant increase of degrees of freedom in the atomic positions, enables the relaxation of the strain in Ho and Y perovskites. The situation for R = Dy is intermediate, with no splitting of the peaks, which suggests that the symmetry of the lattice is orthorhombic.

The Lorentzian contribution to the peak shape is strongly d* dependent, which indicates that it is mainly due to microstrains, and we have not observed a Lorentzian−Scherrer broadening. Despite their different d^* dependences, it is difficult to isolate the two effects as the coherent domains between the stacking faults should result in a "small" Scherrer broadening (due to the small size of the coherent diffraction domains between structural mistakes). In our case, since we have collected data up to a high value of $\sin\Theta/\lambda$, which allows a distinction between these two broadening types, the Scherrer contribution was almost negligible. However, a deep characterization of the structural mistakes for large R cations, using electron microscopy and SXRD data, is underway and it will be reported elsewere.

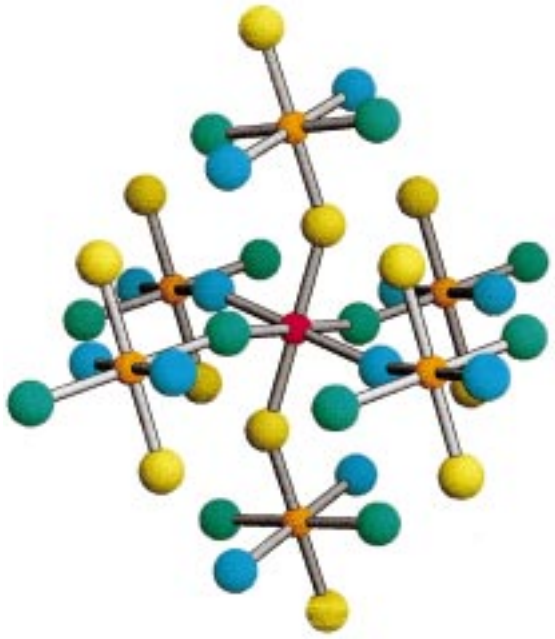

Figure 6. View of the monoclinic $HoNiO_3$ structure, showing the alternation of $Ni1O_6$ and $Ni2O_6$ octahedra. Ni1 and Ni2 are red and orange respectively; O1, O2 and O3 are represented as yellow, green, and blue spheres. For the sake of clarity, Ho atoms are not shown.

Table 7. Mean Tilting Angles of NiO_6 Octahedra (deg), Mean Ni−O and R−O Distances (Å), Tolerance *t* Factors and Unit-Cell Volumes (Å^3) for $RNiO_3$ Perovskites

R	ref	⟨ϕ⟩	⟨Ni−O⟩	⟨R−O⟩	*t*	*V*
La	2,3	7.4	1.934(1)	2.632(1)	0.962	339.06(2)[a]
Pr	2,3	10.7	1.942(1)	2.541(3)	0.925	222.36(1)
Nd	2,3	11.5	1.942(3)	2.514(6)	0.915	220.71(1)
Sm	this work	13.7	1.954(4)	2.471(7)	0.894	218.929(6)
Eu	this work	14.2	1.955(4)	2.451(6)	0.887	217.810(6)
Gd	this work	14.7	1.956(4)	2.438(6)	0.881	216.749(5)
Dy	this work	16.1	1.961(3)	2.406(5)	0.868	213.535(4)
Ho	this work	16.3	1.958(6)	2.397(4)	0.866	211.977(4)
Y	this work	16.3	1.959(4)	2.395(3)	0.864	211.857(5)

[a] For rhombohedral $LaNiO_3$ (*Rc*, $Z = 6$) the normalized volume corresponding to 4 formula units (to compare with the remaining structures, $Z = 4$) is 226.04(2) Å^3.

The average tilting angle ϕ of the NiO_6 octahedra in $RNiO_3$ can be obtained from the superexchange ⟨Ni−O−Ni⟩ angle θ as $\phi = (180 - \theta)/2$. ϕ values for $RNiO_3$ are listed in Table 7. For the sake of comparison, the same calculation has been performed and included for the other members of the $RNiO_3$ series (R = La, Pr, Nd) for which structural data are available. A progressive increase of the tilting angle is observed as the rare-earth size decreases. The relative distortion of the $RNiO_3$ perovskites along the series can also be discussed in terms of the tolerance factor, defined as $t = d_{R-O}/\sqrt{2}d_{Ni-O}$,[18] in the framework of a purely ionic model. Below $t = 1$ (corresponding to the cubic aristotype), the smaller *t* is, the more distorted is the structure. Table 7 also includes the average ⟨Ni−O⟩ and ⟨R−O⟩ bond distances, the tolerance factors and the unit-cell volumes of the $RNiO_3$ perovskites. A gradual decrease of *t* values is observed along the series, as expected.

(18) Goodenough, J. B.; Longo, J. M. In *Magnetic and Other Properties in Oxides and Related Compounds*; Hellwege, K. H., Hellwege, A. M., Eds.; Springer-Verlag: Berlin, 1970; Landolt-Börnstein, New Series, Group III, Vol. 4a, Chapter 3, p 126.

Table 8. Valences Determined from the Bond Valence Model[a] for R, Ni, and O within the RO_8 and NiO_6 Coordination Polyhedra in $RNiO_3$

R	Sm	Eu	Gd	Dy	Ho	Y
R	3.03(2)	3.06(1)	3.09(2)	3.13(2)	3.091(15)	3.03(1)
Ni1	2.908(16)	2.900(15)	2.893(13)	2.86(1)	2.534(16)	2.615(10)
Ni2					3.28(2)	3.169(13)
O1	1.968(16)	2.025(15)	2.035(13)	2.077(13)	2.085(14)	2.066(8)
O2	1.984(15)	1.966(14)	1.973(12)	1.957(11)	1.971(13)	1.93(1)
O3					1.940(14)	1.921(9)
GII	0.052	0.062	0.072	0.104	0.229	0.179

[a] The valence is the sum of the individual bond valences (s_i) for R−O and Ni−O bonds. Bond valences are calculated as $s_i = \exp[(r_0 - r_i)/B]$; $B = 0.37$, $r_0 = 1.686$ for the $Ni^{3+}-O^{2-}$ pair; for the $R^{3+}-O^{2-}$ pairs, from Sm to Y, $r_0 = 2.088$, 2.074, 2.065, 2.036, 2.023, 2.014, from ref 20. Individual R−O and Ni−O distances (r_i) are taken from Tables 3 and 4. The global instability index (GII) is calculated as the root mean of the valence deviations for the $j = 1...N$ atoms in the asymmetric unit, according to $GII = (\sum_j[\sum_i(s_{ij} - V_j)^2]/N)^{1/2}$.

As shown in Table 7, average Ni−O bond distances show a trend to progressively increase, from $SmNiO_3$ to $DyNiO_3$, despite the observed decrease in the lattice volume as R becomes smaller. This behavior can be correlated with the chemical nature of the rare-earth cations present in the $RNiO_3$ phases.[4] For smaller, more acid R^{3+} cations as a partner, the highly charged Ni^{3+} cations are less stable: along the R−O−Ni bonds, the electron density is increasingly kept in the progressively more covalent R−O bonds, thus weakening (lengthening) the Ni−O bonds. From this point of view, the calculation of the valence of the cations and anions present in the solid, following the Brown's bond valence model,[19,20] is enlightening. This model gives a phenomenological relationship between the formal valence of a bond and the corresponding bond length. In ideal nonstrained structures, the bond valence sum (BVS) rule states that the formal charge of the cation (anion) is equal to the sum of the bond valences around this cation (anion). This rule is satisfied only if the stress introduced by the coexistence of different structural units can be relieved by the existence of enough degrees of freedom in the crystallographic structure. The departure of the BVS rule is a measure of the existing stress in the bonds of the structure. The overall stress can be quantified by means of a global instability index (GII),[21] calculated as the root mean of the valence deviations for the $j = 1...N$ atoms in the asymmetric unit, according to $GII = (\sum_j[\sum_i(s_{ij} - V_j)^2]/N)^{1/2}$.

Table 8 lists the valences calculated for R, Ni, and O atoms from the individual R−O and Ni−O bond distances of Tables 4 and 5, as well as GII values. Figure 7 plots the variation of the R and Ni valences vs the ionic radius of R.[22] Rare-earth atoms exhibit valences somewhat higher than the expected value of +3; a trend to increase this valence from Sm to Dy is observed. The opposite behavior is exhibited by Ni valence, which is always below 3+ in the orthorhombic perovskites. This fact seems to indicate that Ni cations are slightly underbonded and hence Ni−O bonds are under tensile stress, whereas R cations are overbonded and under compressive stress, giving rise to a structure with some metastable character: in fact, GII values very quickly increase from R = Sm to R = Dy.

The transition to the monoclinic perovskite for R = Ho and Y leads to a sudden decrease of the Ni1 valence, accompanied by an increment of the Ni2 valence above 3+. As a consequence, GII abruptly increases for both monoclinic, highly

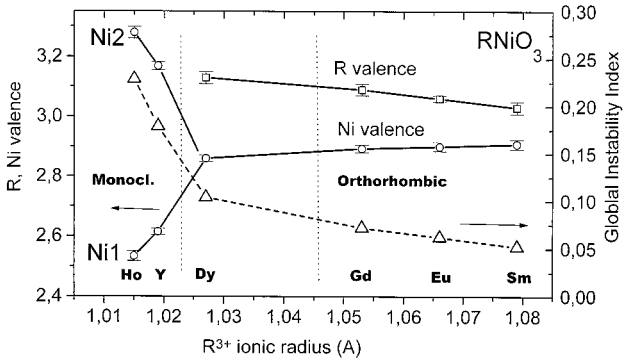

Figure 7. Variation of the valences for R and Ni and global instability index as a function of R^{3+} ionic radius.[21]

metastable perovskites. The occurrence of ordered alternating $3 + \delta$, $3 - \delta'$ valences for Ni cations along the three crystallographic directions suggests the presence of a spin-density-wavelike state indicative of a different electronic ground state at Ni1 and Ni2 cations, in the room-temperature insulating regime. This finding constitutes the first observation of a charge disproportionation in the insulating state of pure and stoichiometric (undoped) $RNiO_3$ perovskites. A self-doping process, in which a fraction of charge leaves Ni2 in favor of their neighboring Ni1 cations, seems to develop in the most distorted perovskites. The disproportionation could be interpreted naturally as the formation of a charge-density wave in which a cooperative oxygen displacement introduces $Ni^{3+\delta}-O\cdots Ni^{3-\delta}$ interactions in all three crystallographic directions. We conclude that in $RNiO_3$ (R = Y, Ho) the establishment of a charge disproportionation is the driving force for the monoclinic distortion observed in the insulating regime.

In contrast with the almost regular NiO_6 octahedra observed in $RNiO_3$ for the largest rare earths (R = La, Pr, Nd)[3], an increasing distortion is observed in the NiO_6 octahedra from $SmNiO_3$ to $DyNiO_3$. For orthorhombic $DyNiO_3$, Ni−O bond distances range between 1.936(2) and 1.986(4) Å, and this distortion is still more pronounced for monoclinic $HoNiO_3$ and $YNiO_3$, in which the two different kinds of NiO_6 octahedra are fairly distorted. The relative distortion of the octahedra can be quantified by the Δ_d parameter, concerning the deviation of Ni−O distances with respect to the average ⟨Ni−O⟩ value. For the sake of comparison, for Pr and Nd nickelates Δ_d values are as small as 10^{-7} and 3×10^{-6}, respectively. As shown in Tables 4 and 5, Δ_d regularly increases (excepting for $EuNiO_3$), from $SmNiO_3$ to $HoNiO_3$, taking values as high as 1.66×10^{-4} for Ni1 in $HoNiO_3$. This effect suggests the progressive manifestation of a cooperative Jahn−Teller (JT) effect along the series. In $RNiO_3$, Ni^{3+} is a JT ion with a single electron in an orbitally degenerate ground state ($t^6_{2g}e^1_g$). The fact that no anisotropy could be detected in the NiO_6 octahedra for the largest rare-earth cations (R = La, Pr, Nd) was thought to be due to the strongly covalent character of the Ni−O bonds. The progressive reduction of this covalent contribution along the series (leading to longer, weaker Ni−O bonds) could explain the increased anisotropy of NiO_6 octahedra as a consequence of the manifestation of JT-induced distortions. In this context, it is important to underline that the existence of JT polarons in stoichiometric charge-transfer $RNiO_3$ systems has been recently demonstrated for lighter rare-earth terms,[8,23] which gives strong support to the polaronic picture suggested for other perovskite oxides containing JT transition-metal cations.[24,25] In $RNiO_3$ oxides, for

(19) Brown, I. D. *Structure and Bonding in Crystals;* O'Keefe, M., Navrotsky, A., Eds.; Academic Press: New York, 1981; Vol. 2, pp 1−30.
(20) Brese, N. E.; O'Keefe, M.; *Acta Crystallogr. Sect. B* **1991**, *47*, 192.
(21) Brown, I. D. *Z. Kristallogr.* **1992**, *199*, 255.
(22) Shannon, R. D.; *Acta Crystallogr. A* **1976**, *32*, 751.
(23) Massa, N. E.; Alonso, J. A.; Martínez-Lope, M. J. *Phys. Rev. B* **1997**, *56*, 986.

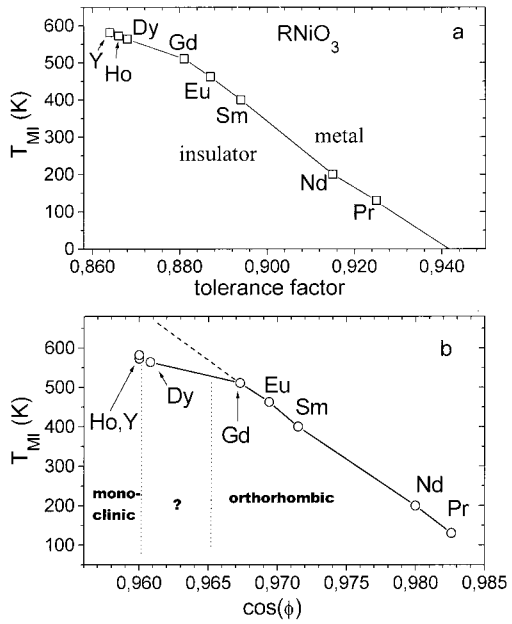

Figure 8. Variation of the MI transition temperature as a function of (a) tolerance factor of the perovskite structure, which gives an idea of the overall distortion and (b) cos ϕ, which is proportional to the bare bandwidth in the absence of structural modifications.

sufficiently small R^{3+} cations, the electron−lattice interactions seem to be strong enough to drive a reduction in crystal symmetry involving a splitting in the Ni^{3+} positions, both placed in significantly distorted octahedral positions.

Figure 8a shows the variation of T_{MI} temperatures vs the tolerance factor of the perovskite structures. The T_{MI} values for R = Pr, Nd, Sm, Eu have been included for the sake of comparison, taken from refs 2 and 4. It has been recently shown[8] that the evolution of T_{MI} along the series can be explained by using the dependence of the bare bandwidth W_b with the structural parameters. For values of the superexchange angle θ close to 180° (as is the case in Ni perovskites), W_b is proportional to $\cos\phi/d^{3.5}_{Ni-O}$, where ϕ is the tilting angle of the NiO_6 octahedra. Disregarding the small variation of d_{Ni-O} along the series of nickelates, the relevant parameter in tuning the bare bandwidth is $\cos\phi$. This approach is not strictly valid when other parameters, such as an additional distortion of the structure, contribute to change W_b. In Figure 8b the linear variation of T_{MI} vs $\cos\phi$ already observed[8] for R = Pr to R = Eu also includes the new datum for R = Gd. However, it is remarkable that the slope significantly decreases for R = Dy, Ho, Y, i.e., the T_{MI} values increase more slowly than expected from the observed variation of the Ni−O−Ni angles. The structural transition toward a more distorted monoclinic crystal structure for $HoNiO_3$ and $YNiO_3$ could be in the origin of this effect. The fact that T_{MI} for the Dy compound seems to fall off of linear correlation found for the orthorhombic nickelates $RNiO_3$, R = Pr...Gd, suggests that $DyNiO_3$ could also exhibit a very subtle monoclinic distortion at room temperature or a different behavior. This distortion, if existent, is not metrically detected in our SXRD data. Furthermore, the microstructure of the sample is very similar to those shown by orthorhombic samples and different from that of monoclinic $RNiO_3$. In the tentative phase diagram showed in Figure 7, $DyNiO_3$ is placed in the boundary between the last "clear" orthorhombic perovskite, $GdNiO_3$, and the first monoclinic perovskite, $HoNiO_3$, in the insulating regime. Neutron powder diffraction data are needed to assess the symmetry of $DyNiO_3$.

High-temperature high-resolution SRXD data have already been collected through the metal−insulator transitions, to characterize the structural and microstructural changes undergone with electron delocalization. The results will be reported elsewhere.

Conclusions

A room temperature study of the structural evolution of $RNiO_3$ (R = Sm, Eu, Gd, Dy, Ho, Y) from SXRD data shows a gradual increase of the structural distortion which leads, for the more distorted Ho and Y phases, to a structural transition toward a monoclinic polytype with two crystallographically independent nickel atoms. The progressive manifestation of the Jahn−Teller effect along the series demostrates the importance of the electron−lattice interaction in the most distorted members of the nickelates series. The significantly different mean Ni−O bond distances observed for Ni1 and Ni2 atoms in the monoclinic phases suggest the presence of a charge disproportionation, commensurate with the crystallographic unit cell. We propose that the presence of a charge-density wave, in the room-temperature insulating regime, is the driving force for the observed lowering in symmetry for the most distorted perovskites (R = Y, Ho). The MI transitions of $RNiO_3$, R = Gd, Dy, Ho and Y, have been measured: The MI temperature for $GdNiO_3$ follows the linear variation with $\cos\phi$ observed for $RNiO_3$ with larger R^{3+} cations ($\cos\phi$ being proportional to the bare bandwidth), but the expected variation rate decreases for R = Dy, Ho and Y. This is consistent with the change of symmetry for $HoNiO_3$ and $YNiO_3$ and suggests that $DyNiO_3$, located at the boundary region between the orthorhombic and monoclinic perovskites, has an anomalous intermediate behavior.

Acknowledgment. We thank Dr. Eric Dooryhee for assistance during data collection on BM16 and for fruitful discussions and to ESRF and ILL for the provision of synchrotron and neutron facilities. The work at Madrid was supported by CICyT, project PB97-1181. The work at Málaga was supported by the research grant FQM-113 of Junta de Andalucía (Spain).

JA984015X

(24) Zhao, G. M.; Conder, K; Keller, H; Muller, K. A. *Nature (London)* **1996**, *381*, 676.

(25) de Teresa, J. M.; Ibarra, M. R., Algarabel, P. A.; Ritter, C.; Marquina, C.; Blasco, J.; García, J.; del Moral, A.; Arnold, Z. *Nature (London)* **1997**, *386*, 256.